



## Two-dimensional numerical modeling of interaction of micro-shock wave generated by nanosecond plasma actuators and transonic flow



M. Abdollahzadeh<sup>a,\*</sup>, J.C. Páscoa<sup>a</sup>, P.J. Oliveira<sup>b</sup>

<sup>a</sup> Universidade da Beira Interior, Departamento de Engenharia Electromecânica, Centre for Aerospace Science and Technologies (CAST), R. Marques D Ávila e Bolama, 6201-001, Covilhã, Portugal

<sup>b</sup> Universidade da Beira Interior, Departamento de Engenharia Electromecânica, Centro Da Estudos de Fenomenos de Transporte (CEFT), R. Marques D Ávila e Bolama, 6201-001, Covilhã, Portugal

### ARTICLE INFO

#### Article history:

Received 29 September 2013

Received in revised form 10 December 2013

#### Keywords:

Nanosecond DBD actuators  
Plasma energy deposition model  
Flow control  
Transonic flow

### ABSTRACT

The influence of nanosecond pulse-driven, surface-mounted dielectric barrier discharge (DBD) actuators on a transonic flow is studied numerically. An airfoil representing turbo-machinery blades in transonic flow is considered as a test case. A two-dimensional fluid model of DBD is used to describe the plasma dynamics. The model couples fluid discharge equations with compressible Navier–Stokes equations. Simulations were conducted with an airfoil of NACA 3506 profile in a transonic condition of  $M = 0.75$ . When a nanosecond pulse voltage is used, with a rise and a decay time of the order of nanoseconds, a significant amount of energy is transferred in a short time from the plasma to the fluid, which leads to the formation of micro-shock waves and therefore to the modification of flow features. Moreover, a plasma energy deposition model is developed and presented by using the results of the plasma discharge model.

© 2013 Elsevier B.V. All rights reserved.

### 1. Introduction

For future huge airships, which are being designed to fly at very high altitude (as in the case of the MAAT project [1]), efficiency increase is a crucial subject. For such airships, any increase in propulsion system efficiency will lead to a decrease in energy consumption through a decrease in size, length and mechanical complexity of propulsion system, thus also lowering the initial investment. At the blades of a propulsion system, separation causes significant total pressure loss causing a reduction in overall efficiency.

The abilities of traditional flow control techniques are limited due to a strict localization and slow response of such systems.

Surface dielectric barrier discharges (SDBDs) can modify the boundary layer of a flow and have been studied as possible actuators for flow control. Their advantages include fast response, real-time control, low weight and no moving mechanical parts. In many applications, airflow control by DBD actuators is based on the generation of the ionic wind at the wall which adds momentum to the boundary layer. At low flow velocities, those actuators have proven to be effective for a wide range of applications [2,3]. At high flow velocities, however, the effect of the induced wall jet is almost negligible. In our previous study [4], the interaction between an AC-driven DBD actuator mounted on a NASA rotor 67 blade profile in transonic flow was

\* Corresponding author. Tel.: +351 925467631; fax: +351 275329972.  
E-mail address: [mm.abdollahzadeh@yahoo.com](mailto:mm.abdollahzadeh@yahoo.com) (M. Abdollahzadeh).

### Nomenclature

$C_p$	Specific heat capacity ( $\text{J kg}^{-1} \text{K}^{-1}$ )
$n$	Charge particle density ( $\text{m}^{-3}$ )
$t$	Time (s)
$r$	Recombination coefficient ( $\text{m}^3 \text{s}^{-1}$ )
$D$	Charged particle diffusion coefficient ( $\text{m}^2 \text{s}^{-1}$ )
$e$	Electron charge ( $1.6 \times 10^{-19} \text{C}$ )
$\vec{j}$	Total electric current ( $\text{Am}^{-2}$ )
$\vec{J}$	Conduction current ( $\text{Am}^{-2}$ )
$\vec{n}$	Unit normal vector
$p$	Pressure ( $\text{N m}^{-2}$ )
$k_B$	Boltzmann constant ( $\text{m}^2 \text{kg s}^{-2} \text{K}^{-1}$ )
$m$	Mass of particle (kg)
$T$	Temperature (K)
$\eta_E$	Fractional power deposited in electronic excitation
$\eta_V$	Fractional electron power deposited in vibrational excitation
$\eta_{el-R}$	Fractional electron power deposited in elastic and rotational excitation
$\sigma_e$	Electron conductivity ( $\text{S m}^{-1}$ )
$\sigma$	Surface charge density ( $\text{C m}^{-2}$ )
$\mu_i$	Charged particle mobility ( $\text{m}^2 \text{V}^{-1} \text{s}^{-1}$ )
$\mu$	Fluid dynamic viscosity ( $\text{Pa s}$ )
$\phi$	Electric potential (V)
$\rho$	Density ( $\text{kg m}^{-3}$ )
$\vec{\Gamma}$	Charged particle flux ( $\text{m}^{-3} \text{s}^{-1}$ )
$\varepsilon$	Permittivity ( $\text{Fm}^{-1}$ )
$\delta$	Delta function
$\gamma$	Secondary electron emission
$E$	Total specific energy ( $\text{J kg}^{-1}$ )
$\vec{F}_{EHD}$	Electric force density ( $\text{N m}^{-3}$ )
$p_{th}$	Electric power density ( $\text{W m}^{-3}$ )
$I$	Unity tensor
$R$	Air specific gas constant ( $\text{J kg}^{-1} \text{K}^{-1}$ )
$\vec{u}$	Velocity of gas flow ( $\text{ms}^{-1}$ )
$\vec{E}$	Electric field vector, ( $\text{kg.m.s}^{-3}.\text{A}^{-1}$ )

### Greek symbols

$\alpha$	Ionization coefficient, ( $\text{m}^{-1}$ )
$\eta$	Attachment coefficient ( $\text{m}^{-1}$ )
$\nu$	Kinematics viscosity ( $\text{N s m}^{-2}$ )
$\tau$	Viscous stress tensor
$\tau_{VT}$	Relaxation of time for vibrational excitation (s)
$\kappa$	Thermal conductivity ( $\text{W m}^{-1} \text{K}^{-1}$ )
$\xi$	Effective fraction of energy deposition

### Subscripts

$e$	Electron
$p$	Positive ion
$n$	Negative ion
$s$	Surface
$d$	Dielectric
$0$	Reference state

investigated and almost no noticeable effect of the actuator on the performance of the rotor was observed. Recently [5,6], it was shown that a DBD actuator driven by nanosecond (NS) pulse has a more significant impact on the transonic flow. It was found that in these types of DBD actuators, there is an overheating in the discharge region, which generates a compression wave emerging from the surface into the flow. In this case, the effective control of the flow implies an appreciable change

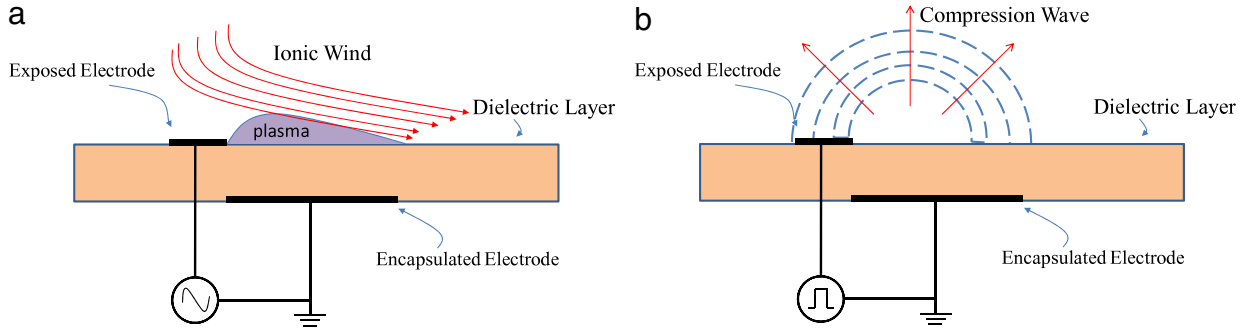


Fig. 1. DBD Plasma Actuators (a) AC sinusoidal power source (b) NS power source.

in its properties by local energy deposition. Fig. 1 shows the two main approaches by which DBD plasma actuators may influence the flow.

The purpose of the present study is to describe a numerical model for a surface dielectric barrier discharge in air, which uses a nanosecond voltage pulse generator. A two-dimensional fluid model of the DBD is used to describe the plasma dynamics at first. The model couples the fluid discharge equations with the compressible Navier–Stokes equations, which include momentum and thermal transfer from the plasma to the neutral gas. The 2D fluid model of the discharge in air provides the space and time evolution of the charged particle densities, electric field and surface charges. The model is solved numerically by means of a finite volume technique. A validation of the model is presented in order to assess the capabilities of the computational code here developed. Secondly, a new plasma energy deposition model is presented based on the analysis of the results of the discharge model.

The remainder of this paper is organized in four sections. Section 2, presents the governing equations and the numerical procedure related to the modeling of the plasma discharge and the energy deposition model. In Section 3 the details of the configuration here considered for the test cases in the numerical experiments are provided. In Section 4, comparison and analysis of the obtained numerical results are presented. Finally, in Section 5, some important conclusions are drawn.

## 2. Mathematical model and numerical procedure

### 2.1. Plasma discharge mathematical model

In this model we are not interested in the details of air chemistry and, for the purpose of simplification, we just consider three types of charged particles: electrons, one type of generic positive ion, and one type of generic negative ion. By considering the fluid description of electron and ion transport in air by means of classical drift-diffusion and local field approximation, the continuity equations for the electrons and the ions are written as

$$\frac{\partial n_e}{\partial t} + \nabla \cdot \vec{\Gamma}_e = (\alpha - \eta) \|\vec{\Gamma}_e\| - r_{ep} n_e n_p, \quad (1)$$

$$\frac{\partial n_p}{\partial t} + \nabla \cdot \vec{\Gamma}_p = \alpha \|\vec{\Gamma}_e\| - r_{ep} n_e n_p - r_{np} n_n n_p, \quad (2)$$

$$\frac{\partial n_n}{\partial t} + \nabla \cdot \vec{\Gamma}_n = \eta \|\vec{\Gamma}_e\| - r_{np} n_n n_p, \quad (3)$$

$$\vec{\Gamma}_i = -\mu_i n_i \vec{E} - D_i \nabla n_i + n_i \vec{u}, \quad (4)$$

where  $n_e$ ,  $n_p$ ,  $n_n$  are the charged particle densities,  $\vec{\Gamma}_i$ ,  $i = e, p, n$  their fluxes, and  $\alpha$ ,  $\eta$ ,  $r_{np}$  and  $r_{ep}$  are, respectively, the ionization coefficient, the attachment coefficient, ion–ion and electron–ion recombination coefficients. Moreover  $\vec{E}$  is the electric field vector,  $\mu_i$  and  $D_i$  are the charged particle mobility and diffusion coefficients, respectively, and  $\vec{u}$  is the velocity of the gas flow. The recombination coefficients are considered to be constant and equal to  $10^{-13} \text{ m}^3 \text{ s}^{-1}$  [7]. The charged particle mobility and ionization coefficients of the air are obtained from Hoskinson [7] and are written as

$$\mu_e (\text{m}^2 \text{ Torr V}^{-1} \text{ s}^{-1}) p = 0.21 \left[ 24.32 \exp\left(\frac{-E/p}{1057}\right) + 19.38 \exp\left(\frac{-E/p}{23430}\right) + 14.45 \right] \\ + 0.79 \left[ 173.1 \exp\left(\frac{-E/p}{195.1}\right) + 36.19 \exp\left(\frac{-E/p}{12763}\right) + 31.73 \right], \quad (5)$$

$$\mu_p (\text{m}^2 \text{Torr V}^{-1} \text{s}^{-1}) p = 0.79 \left[ 0.05492 \exp \left( \frac{-E/p}{6858} \right) + 0.07509 \exp \left( \frac{-E/p}{38175} \right) + 0.0308 \right] + 0.21 \left[ 0.06841 \exp \left( \frac{-E/p}{59678} \right) + 0.09194 \exp \left( \frac{-E/p}{12763} \right) + 0.0320 \right], \quad (6)$$

$$\frac{\alpha}{p} = 0.21 \left[ \begin{cases} 4.71 \times 10^{-11} |E/p|^3, & |E/p| < 1.4 \times 10^4 \text{ V m}^{-1} \text{ Torr}^{-1} \\ 3.32(|E/p| - 12500)^{0.5}, & |E/p| > 1.4 \times 10^4 \text{ V m}^{-1} \text{ Torr}^{-1} \end{cases} \right] + 0.79 \left[ \begin{cases} 1.17 \times 10^{-10} |E/p|^3, & |E/p| < 1.1 \times 10^4 \text{ V m}^{-1} \text{ Torr}^{-1} \\ 0.0319 |E/p| - 211, & 1.1 \times 10^4 < |E/p| < 2.1 \times 10^4 \text{ V m}^{-1} \text{ Torr}^{-1} \\ 6.32(|E/p| - 16300)^{0.5}, & |E/p| > 2.1 \times 10^4 \text{ V m}^{-1} \text{ Torr}^{-1} \end{cases} \right]. \quad (7)$$

The charged particle diffusion coefficients in Eqs. (1)–(3) are expressed by the Einstein relation and the charged particles temperature in the diffusion terms are taken as constant, 1 eV for the electrons and 350 K for the ions.

Eqs. (1)–(4) are coupled to a Poisson equation for the electric field:

$$\nabla \cdot (\varepsilon \nabla \phi) = -e(n_p - n_e - n_n) - \delta_s \sigma, \quad (8)$$

where  $\varepsilon$  is the permittivity. The permittivity of air is considered to be equal to that of vacuum ( $\varepsilon_0 = 8.854 \times 10^{-12} \text{ Fm}^{-1}$ ) and  $\sigma$  is the surface charge density in  $\text{kg s}^{-3} \text{ A}^{-1}$  this is evaluated at the dielectric surface, as indicated by the delta function  $\delta_s$ , after time integrating the charged particle fluxes at the surface:

$$\sigma = \int_0^t -e (\vec{\Gamma}_p - \vec{\Gamma}_e - \vec{\Gamma}_n) \cdot \vec{n} dt = \int_0^t -\vec{j} \cdot \vec{n} dt, \quad (9)$$

where  $\vec{n}$  is the unit normal vector pointing into the computational domain. For the electric field at the outer boundaries, the following condition is held:

$$\vec{E} \cdot \vec{n} = 0, \quad (10)$$

and at the electrode, the value of electric potential is prescribed. The electric field inside the dielectric  $\vec{E}_d$  was related to the electric field  $\vec{E}$  at the surface through the relation

$$\varepsilon_0 \vec{E} \cdot \vec{n} - \varepsilon_d \varepsilon_0 \vec{E}_d \cdot \vec{n} = \sigma, \quad (11)$$

where  $\sigma$  is the surface charge density and  $\vec{n}$  is the unit normal vector pointing into the computational domain. By implementing this condition, the effect of the surface charge density in the continuity equation is taken into account. In addition zero normal gradients are considered for the boundary conditions of the charged particles at outer boundaries.

The boundary conditions for charged particle number density at the walls are set out by preventing zero charged particle fluxes towards the wall, since the driving forces are directed outwards from it, and by enforcing ion-induced secondary emission at cathode or cathode-like walls:

$$\vec{\Gamma}_p \cdot \vec{n} = -\frac{1}{4} \sqrt{8 \frac{k_B T_p}{\pi m_p} + n_p} \left[ \min(\mu_p \vec{E} \cdot \vec{n}, 0) \right] \cdot \vec{n}, \quad (12)$$

$$\vec{\Gamma}_e \cdot \vec{n} = -\frac{1}{4} \sqrt{8 \frac{k_B T_e}{\pi m_e} + n_e} \left[ \min(-\mu_e \vec{E} \cdot \vec{n}, 0) \right] \cdot \vec{n}, \quad (13)$$

$$\vec{\Gamma}_n \cdot \vec{n} = -\frac{1}{4} \sqrt{8 \frac{k_B T_n}{\pi m_n} + n_n} \left[ \min(-\mu_n \vec{E} \cdot \vec{n}, 0) \right] \cdot \vec{n}. \quad (14)$$

For certain cases, these boundary conditions lead to numerical instability. For anode or anode-like surfaces, the boundary condition that would satisfy the real situation for negative ions and electrons is one of zero gradient on the electron number density. The derived boundary condition on ions at an anode is a Robin condition for the number density of ions. (However, since the diffusion is always negligible with respect to its drift part in the sheath, it is possible to employ a more robust and simpler condition [8], namely  $n_p = 0$ .)

On the other hand, for the cathode or cathode-like surfaces, the zero gradient boundary condition could satisfy the condition for the positive ion number density. Here, the boundary condition on electrons is a Robin condition (for simplification, it is possible to neglect the diffusion part). Electrons may be emitted from material surfaces via secondary electron emission. Therefore, the total electron flux near a surface is given by

$$\vec{\Gamma}_e \cdot \vec{n} = -\gamma \vec{\Gamma}_p \cdot \vec{n}, \quad (15)$$

where  $\gamma$  is the secondary electron emission coefficient at the surface, which is 0.05 for the dielectric surface, and zero for electrode surface. The minus sign indicates that secondary electron fluxes, away from a surface, are proportional to the ion fluxes into that surface.

## 2.2. Gas dynamics equations

For modeling the gas dynamics, a mass-averaged fluid dynamical formulation was employed to represent the motion of the gas as a whole. In this view, the compressible Navier–Stokes formulation is written as

$$\frac{\partial \rho}{\partial t} + \nabla \cdot (\rho \vec{u}) = 0, \quad (16)$$

$$\frac{\partial \rho \vec{u}}{\partial t} + \nabla \cdot (\rho \vec{u} \vec{u} + pI - \tau) = \vec{F}_{EHD}, \quad (17)$$

$$\frac{\partial \rho E}{\partial t} + \nabla \cdot ((\rho E + p)\vec{u}) = \nabla \cdot (\kappa \nabla T) + \nabla \cdot (\tau \cdot \vec{u}) + \vec{F}_{EHD} \cdot \vec{u} + p_{th}. \quad (18)$$

In the above equations,  $p$  is the static pressure,  $I$  is the unity tensor,  $\tau$  is the viscous stress tensor,  $E$  is total specific energy and  $\kappa$  is the thermal conductivity of air. The interaction terms are  $\vec{F}_{EHD}$ , force due to discharge, and  $p_{th}$ , the dissipated power due to the conduction current,  $\vec{J} = j - e(n_p - n_e - n_n) \cdot \vec{u}$ . In the above equations the viscous stress tensor is as follows:

$$\tau = \mu \left[ (\nabla u) + (\nabla u)^T - \frac{2}{3} \nabla \cdot \vec{u} I \right], \quad (19)$$

where  $\mu$  is the dynamic viscosity of air and is calculated from Sutherland's formula.

The above system of equation is closed with the equation of state for a perfect gas,  $p = \rho RT$ . Coupling parameters due to plasma effects inside the gas dynamic equations are represented through the EHD force  $\vec{F}_{EHD}$  and the heating power density  $p_{th}$ . The EHD force term is written as [9],

$$\vec{F}_{EHD} = e(n_e - n_p - n_n)\vec{E} - k_B T_p \nabla n_p - k_B T_e \nabla n_e - k_B T_n \nabla n_n. \quad (20)$$

In our previous work, the heating power density  $p_{th}$  was considered to consist of ion–neutral collisions, actually the energy deposited by electron elastic collisions, rotational excitation and vibration excitation, and was written as

$$p_{th} = (\vec{J}_p - \vec{J}_n - \xi \vec{J}_e) \cdot \vec{E}, \quad (21)$$

where  $\xi$  was the effective fraction of energy deposited by electron, considered to be constant and equal to 0.75 [10,11]. However, here we consider a more accurate formulation for the  $p_{th}$  of electrons following Unfer and Boeuf [12]. In this view, the gas heating term is composed of two parts, one contribution of the ion–neutral molecule collisions  $p_{ions}$  and the other the thermal energy transfer from electrons to neutral particles  $p_{th,e}$ . Assuming that all the energy obtained by ions from the electric field is totally transferred into gas heating,  $p_{ions}$  is expressed as

$$p_{ions} = (\vec{J}_p - \vec{J}_n) \cdot \vec{E}. \quad (22)$$

The total energy absorbed by electrons from electric field is equal to  $p_{elec} = \sigma_e E^2$ , where  $\sigma_e$  is the electron conductivity. This energy is transferred to neutral molecules and gas heating through electronic excitation, vibrational excitation and elastic and rotational collisions [13,14]. Moreover, it is assumed that the energy is absorbed by electrons in elastic and rotational excitation, and 30% of the energy in electronic excitation is released instantaneously into gas heating. But, the vibrational excitation of electrons into gas heating is released in a different timescale, with a time constant of  $\tau_{VT}$ . Thus the contribution of electrons in gas heating can be expressed as

$$p_{th,e} = p_{el-R} + p_{VT} + p_E, \quad (23)$$

with

$$\begin{aligned} p_{el-R} &= \eta_{el-R} p_{elec} \\ p_E &= \xi \eta_E p_{elec}, \end{aligned} \quad (24)$$

where  $\eta_E$  is the fractional power deposited in electronic excitation and  $\xi = 30\%$ . In Eq. (23), considering a relaxation of time of  $\tau_{VT}$  for vibrational excitation,  $p_{VT}$  is obtained by solving a phenomenological equation of the type

$$\frac{\partial p_{VT}}{\partial t} + \frac{1}{\tau_{VT}} p_{VT} = \frac{1}{\tau_{VT}} \eta_V p_{elec}, \quad (25)$$

where  $\eta_V$  is the fractional electron power deposited in vibrational excitation of air molecules.

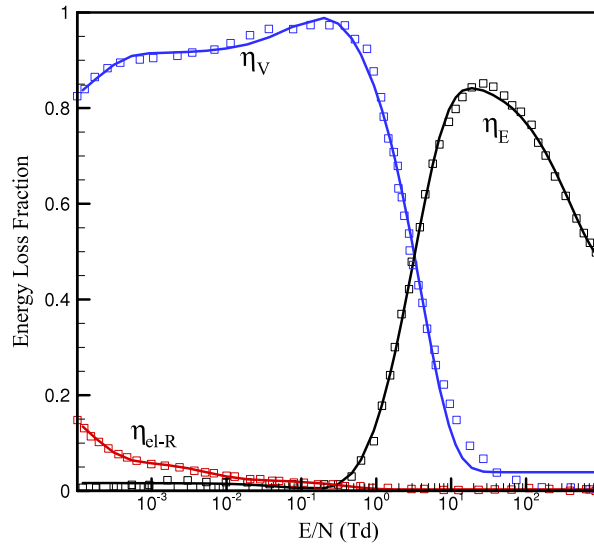


Fig. 2. Comparison fractional power deposited by electrons from the current correlations (Eqs. (26)–(28)) and the data obtained by BOLSIG + software.

The three fractional powers deposited by electron ( $\eta_E$ ,  $\eta_V$ ,  $\eta_{el-R}$ ) are obtained by fitting curves to data calculated as a function of  $E/n$  using BOLSIG + software [15] as (Fig. 2):

$$\begin{aligned} \eta_E = & 1.348001 \times 10^{-1} \exp\left(-3.5410 \left|\frac{E}{N}\right|\right) - 9.8365 \times 10^{-1} \exp\left(-2.02042 \times 10^{-1} \left|\frac{E}{N}\right|\right) \\ & + 4.14522 \times 10^{-1} \exp\left(-2.63147 \times 10^{-3} \left|\frac{E}{N}\right|\right) + 4.507497 \times 10^{-1}, \end{aligned} \quad (26)$$

$$\begin{aligned} \eta_V = & -1.6041 \times 10^{-1} \exp\left(-6.10797 \times 10^{+3} \left|\frac{E}{N}\right|\right) - 1.46957 \times 10^{-1} \exp\left(-9.4288 \left|\frac{E}{N}\right|\right) \\ & + 1.02191 \exp\left(-2.5157 \times 10^{-1} \left|\frac{E}{N}\right|\right) + 3.91435 \times 10^{-2}, \end{aligned} \quad (27)$$

$$\begin{aligned} \eta_{el-R} = & 2.07278 \times 10^{-2} \exp\left(-2.6180 \left|\frac{E}{N}\right|\right) + 4.04597 \times 10^{-2} \exp\left(-1.7446 \times 10^2 \left|\frac{E}{N}\right|\right) \\ & + 1.68412 \times 10^{-1} \exp\left(-7.13103 \times 10^{+3} \left|\frac{E}{N}\right|\right) + 2.98161 \times 10^{-3}. \end{aligned} \quad (28)$$

### 2.3. Surface and volume heating model

Another idea to simplify the numerical complexity and reduce the computational time is to formulate the effect of plasma as volume and surface sources of energy deposition, with a specified frequency inside the flow domain. To this aim, an approach similar to the phenomenological model described in [16–19] is chosen. To reproduce the overall wave structure, wave speed and strength, and power input to the NS-DBD actuators, a surface and volume heating profile is considered in a way to obtain similar results as in the full discharge modeling. The speed and strength of the initial wave is related to the maximum temperature in the heated region, which is obtained by introducing a volume heating component and the shape of the wave correlates with the temperature distribution along the surface. Fig. 3 demonstrates the development of the compression wave due to volume and surface heating. Using a simple analysis, the volume heating can be estimated from

$$Q_{th} = \rho C_v \frac{\Delta T}{t_{E,relax}}. \quad (29)$$

Considering the discharge volume of  $25e - 8 \text{ m}^3$  and temperature ratio increase of 1.4 for the ambient temperature of 300 K, and a relaxation time of  $1 \mu\text{s}$ , we can calculate the power needed per span wise electrode length to actuate the flow as  $2.6 \times 10^4 \text{ W/m}$ , which is equivalent to  $0.026 \text{ J/m}$  by integrating the above equation over volume.

Moreover, the process of formation of the plasma micro-shock wave above the surface is separated into two parts. In the first part, the pulse of energy input to the plasma is started at  $t = 0$  and switched off at  $t_{E,relax}$  (which we consider to be equal to  $1 \mu\text{s}$ ). During this period the pressure and temperature rise above the surface and the wave front moves just a

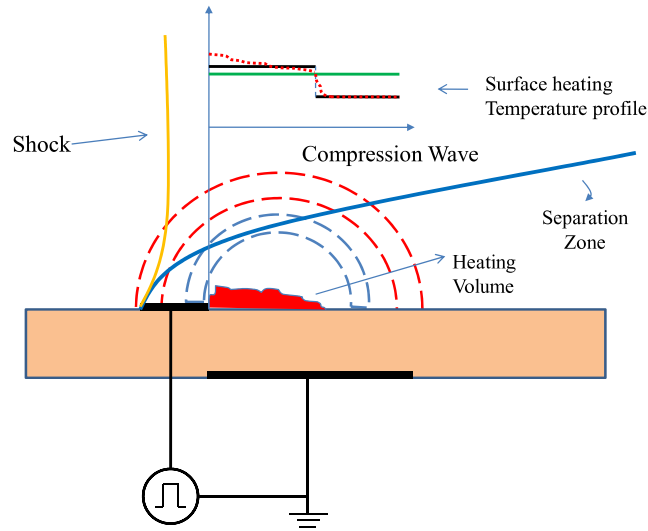


Fig. 3. Schematic of the plasma surface and the volume energy deposition model.

short distance away from the surface. In the second part, when the pulse of energy input is switched off, an expansion wave is generated and propagates into the domain.

#### 2.4. Numerical procedure

The strong coupling between the charge density equations and the electric potential results in a severe time step restriction (the maximum allowable time step is the dielectric relaxation time). In order to overcome this constraint, the Poisson equation is solved in a semi-implicit manner for the electric potential [20],

$$\nabla \cdot (\varepsilon \nabla \phi) = -e \left( n_p^t + \Delta t \frac{\partial n_p}{\partial t} - n_e^t - \Delta t \frac{\partial n_e}{\partial t} \right). \quad (30)$$

In this way the Poisson equation can be rewritten as

$$\nabla \cdot ([\varepsilon + \Delta t (\mu_p n_p + \mu_e n_e)] \nabla \phi) = -e (n_p^t + \Delta t \nabla \cdot (\nabla n_p^t) - \nabla \cdot (n_p \vec{u}) - n_e^t - \Delta t \nabla \cdot (\nabla n_e^t) + -\nabla \cdot (n_e \vec{u})). \quad (31)$$

Further, a two-stage plasma computation approach [21,22] is implemented. In this approach, during the voltage pulse, the numerical time step is set to  $10^{-3}$  ns, and the full physical model solved. When the input voltage decays the electric field effects become negligible and the space charge density rapidly decreases. Therefore, in this stage, the electric field and space charge are set to zero and the time step is increased to the timescale of the dominant physical process (gas dynamics).

The numerical task has been performed through Object Oriented Programming in the environment of OpenFoam by developing a new solver (UBIPlasmaFoam). The solution of the gas dynamic equations was accomplished based on a density based explicit algorithm. The numerical fluxes were evaluated using the flux difference splitting Roe scheme [23] and to extend the accuracy in space, a second order MUSCL reconstruction scheme is used. Integration in time is performed by multistage pseudo time integration based on a four-stage Runge–Kutta method. Moreover, a two parameter  $k-\omega$  SST turbulence model with  $y^+$  less than one is used for the turbulent transfer description [24]. The initial distribution of parameters corresponding to the steady flow around the airfoil without energy addition was obtained with an absolute error of  $10^{-6}$ . The computational grid in the physical region is geometrically adapted towards the wall being refined in the vicinity of the electrode and dielectric surfaces.

### 3. Test case configurations

#### 3.1. Validation cases

For the validation of the numerical modeling of the plasma discharges, two flat plate DBD actuators are considered (similar to [25]). The electrodes were considered to be infinitely thin and arranged in asymmetric configuration without a gap between the electrode edges. Moreover, in the initial time instant, the gas is considered to be quasi-neutral, the initial charged particle densities (electrons and positive ions) are considered to be uniform and equal to  $10^{13} \text{ m}^{-3}$  in the first case and  $10^{10} \text{ m}^{-3}$  in the second case, in the whole simulation domain. In the first configuration, the length of the exposed

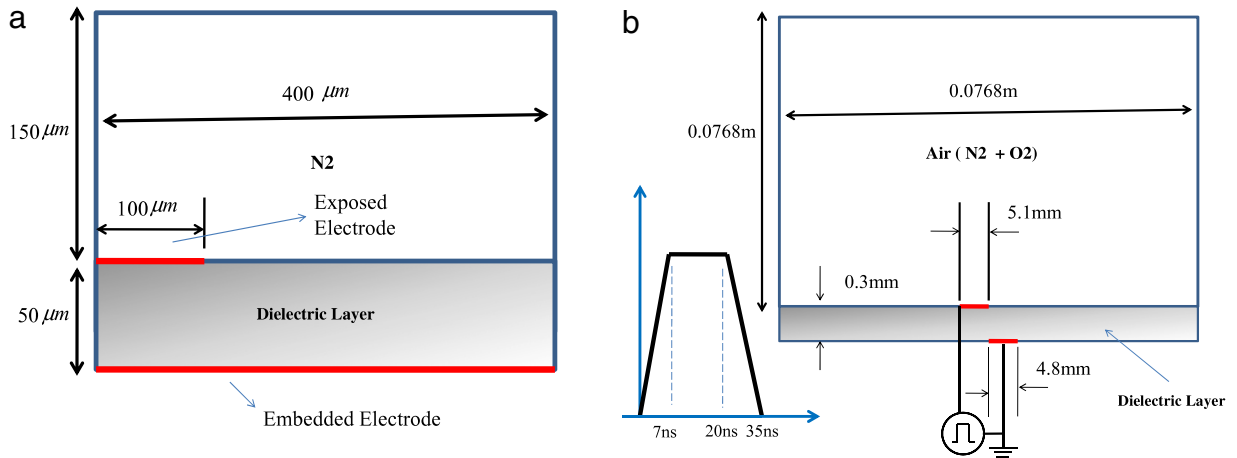


Fig. 4. Configuration of the validation test cases for the present plasma discharge modeling.

electrode and the covered electrode are  $100\ \mu\text{m}$  and  $400\ \mu\text{m}$ , respectively, and a constant voltage of  $1200\ \text{V}$  is applied to the exposed electrode. The dielectric material is Kapton, having electric permittivity of  $10\epsilon_0$  and thickness of  $50\ \mu\text{m}$ .

The second test case is considered in a similar way to the experiment of Straikovskii et al. [5] and the numerical study of Unfer and Boeuf [9]. The computational domain consists of a 2D rectangular geometry, of dimensions  $0.0768\ \text{m} \times 0.0768\ \text{m}$ . The length of the exposed electrode is considered to be  $5.1\ \text{mm}$  and the lower electrode is  $4.8\ \text{mm}$  long. The upper electrode is placed at  $0.03\ \text{m}$  from the left wall. A voltage pulse is applied to the upper electrode. The total pulse duration is  $35\ \text{ns}$  and the rise and falling time of the nanosecond pulse are  $7\ \text{ns}$  and  $15\ \text{ns}$ , respectively. The lower electrode is covered by a dielectric layer  $300\ \mu\text{m}$  thick and permittivity is equal to  $5\epsilon_0$ . The configuration of these test cases is shown in Fig. 4.

### 3.2. Transonic airfoil gas dynamic with plasma dynamic at low and high angle of attack

The transonic range of flying vehicles is the most difficult to simulate in aerodynamics; on the other hand, the feasibility of controlling transonic flows would greatly improve the aerodynamical performance of flying vehicles (and thereby increase the flight range, reduce the carrier cost, etc.) and allow flight control at maneuvering. In this context, Peschke et al. [26] conducted an experimental study on the effect of DBD plasma actuators on transonic flow over a NACA 3506 airfoil. They concluded that the plasma used did not modify the transonic flow in a significant way. The fact that shock structure does not exhibit significant differences without and with plasma can have several physical causes. The boundary layer is already turbulent in the case without plasma. It is thus not possible in these conditions to generate a transition from a laminar boundary layer to a turbulent one with plasma upstream or below the shock foot. However, the results of [27] show that in some cases, when the aerodynamics situation is sensitive to weak influence, the surface plasma of barrier discharge can affect transonic flow. Moreover, Roupasov et al. [28] showed that the discharge effect is negligible until a specified angle of attack and for the angles higher than the stall angle the discharge switches the flow to unseparated flow.

Therefore, for the study of the effect of plasma actuator on gas dynamic, the plasma actuator is mounted on a NACA 3506 profile with a chord length of  $c = 77.57\ \text{mm}$ , similar to the experiment by Peschke et al. [26]. The electrodes are considered to be infinitely thin. The exposed electrode is located at  $x/c = 0.32$  from the leading edge and is  $1\ \text{mm}$  wide, and the covered electrode is  $10\ \text{mm}$  wide. The electrodes are separated by a  $0.1\ \text{mm}$  thick layer of dielectric material. The permittivity of the dielectric material is  $5\epsilon_0$ . A single pulse with a peak voltage of  $V_p = 5\ \text{kV}$  and pulse shape similar to that for the second test case is considered as configuration of the power supply. Two different angles of attack are considered. One corresponds to an angle of attack of  $4^\circ$  and other to a post stall angle of attack of  $20^\circ$ . The configuration of the electrodes and the computational grid for this case are presented in Fig. 5.

## 4. Results and discussions

For the first test case the effect of gas heating is not considered and so the only mechanism by which the plasma modifies the flow is through momentum transfer to the fluid. Figs. 6 and 7 shows a simulation results of the time evolution of the discharge plasma for the case of a constant voltage pulse of  $1.2\ \text{kV}$ . The discharge plasma consists of a quasi-neutral plasma column and a non-neutral ion sheath that propagates along the dielectric surface, away from the exposed electrode. It is obvious from these figures that the discharge is of the streamer type. Our results in Fig. 6 show similar physical behavior in comparison to the results of Nishida and Abe [2] and Bouef and Pitchford [25].

The distribution of ion charge density is shown in Fig. 7. It is apparent that, as the charge density of ions and electrons near the dielectric surface is increased, the electric potential on the surface of the dielectric material is raised, thus increasing the



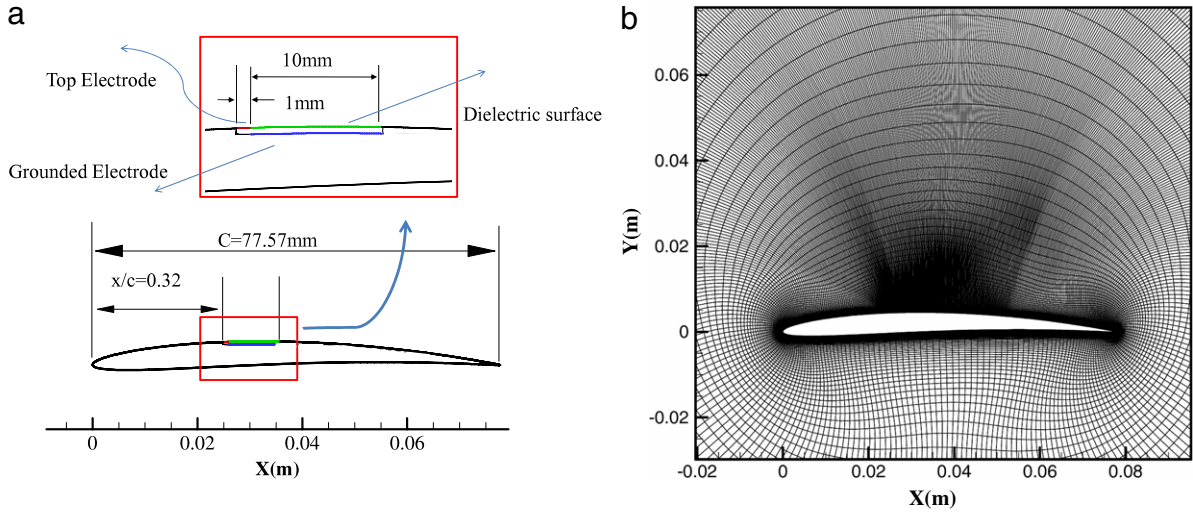


Fig. 5. (a) Electrodes position and (b) computational grid around the surface of the NACA 3506 airfoil.

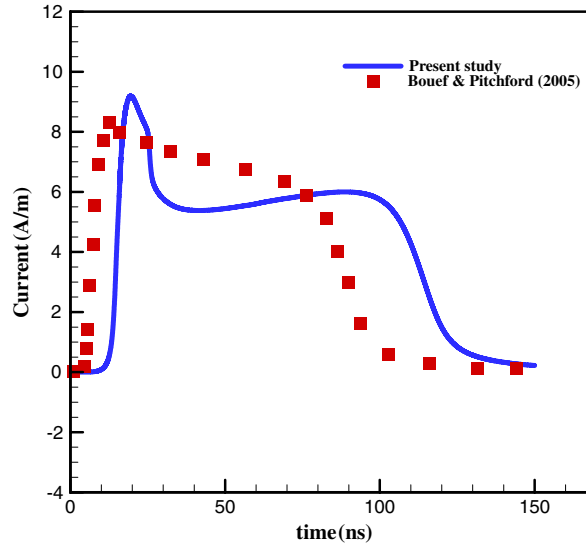


Fig. 6. Validation of the first test case with the numerical results of Boeuf and Pitchford (2005) [25].

extension of the electrode. Fig. 7 also shows that the region with higher ion density is located at the point with the largest electric field, and thus a higher rate of ionization exists there. Fig. 8 illustrates the formation of the wall jet due to addition of momentum to the fluid, in the presence of plasma.

For the second test case the effect of gas heating was taken into account. Fig. 9 shows the general good agreement of the predicted current density, from the present numerical simulation, in comparison with the numerical work of Unfer and Boeuf [9]. Moreover Fig. 10 shows the time evolution of the electron and potential density at four different times. Streamer discharge propagation along the surface of the dielectric was observed during the voltage rise when the exposed electrode plays the role of anode.

Fig. 11 illustrates the spatial distribution of the gas pressure induced by the discharge at two different time instants. These results highlight that fast gas heating takes place in the boundary layer, close to the edge of the exposed electrode, thus producing a micro-shock wave.

Fig. 12 shows the formation of the micro-shock wave above the dielectric surface mounted on the surface of the NACA 3506 airfoil. The formation of the plasma on the surface of the electrode leads to a very fast gas heating of the fluid near the surface, which in this case results in the formation of a compression wave traveling outward from the surface.

In general, the solution of the coupled plasma dynamics and gas dynamics equations together is computationally very expensive. To increase the efficiency of the numerical computations, two different approaches may be adopted, as referred to before. The first is the two-stage plasma calculation technique, and the second is the plasma energy deposition model.

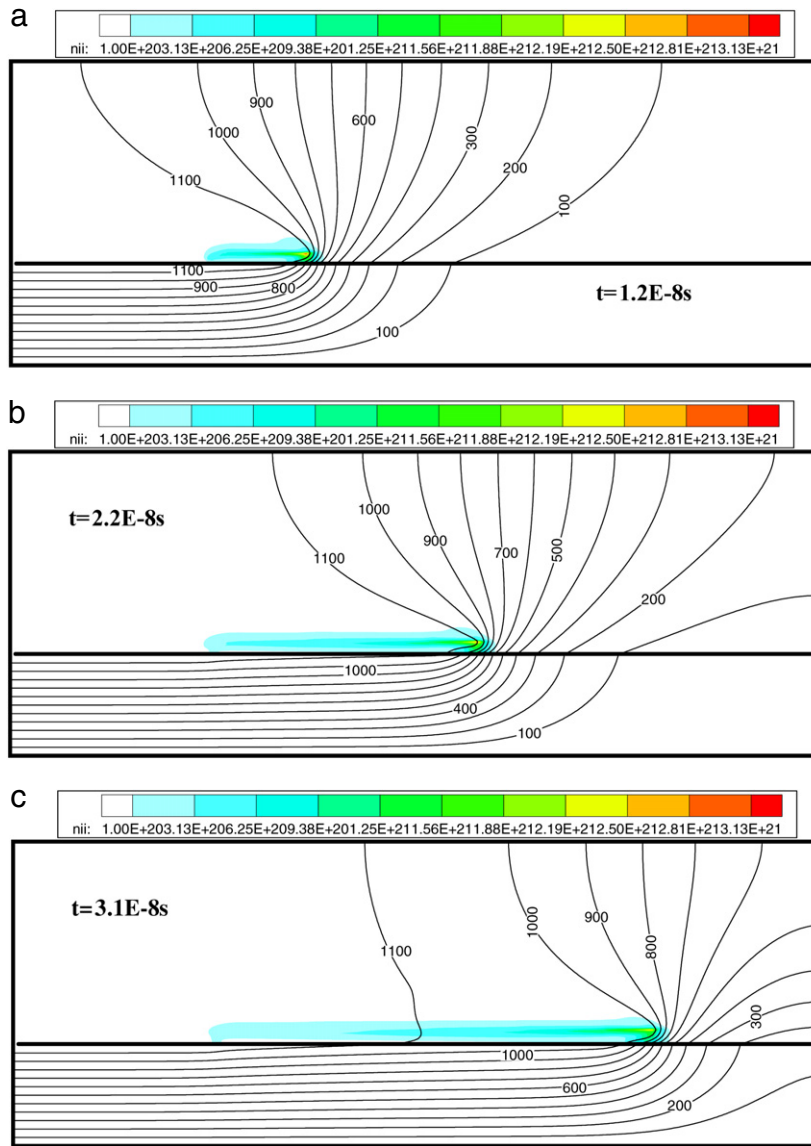


Fig. 7. Propagation of the ion sheath along the dielectric surface at: (a)  $t = 12$  ns; (b)  $t = 22$  ns; (c)  $t = 31$  ns (values of ion charge density in  $\text{m}^{-3}$ ).

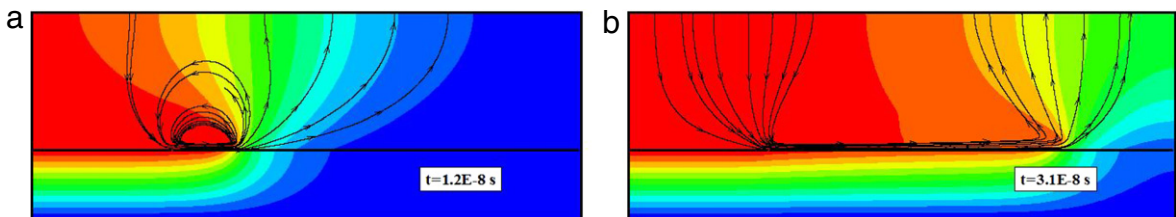


Fig. 8. Wall jet formation beside the dielectric surface at: (a)  $t = 12$  ns; (b)  $t = 31$  ns.

In Fig. 13, the computed temperature profile at the surface dielectric material, for the NACA 3506 airfoil, is shown together with the imposed profile. The surface heating profile is a step profile that has a jump at a critical point  $x_c$ . Two important parameters of this profile are the temperature ratio and the critical step point.

Fig. 14 gives the time evolution of the drag coefficient over the surface of the airfoil until  $70 \mu\text{s}$  as predicted by the two approaches just mentioned. It is clear from this figure that the difference of the computed results by the two different

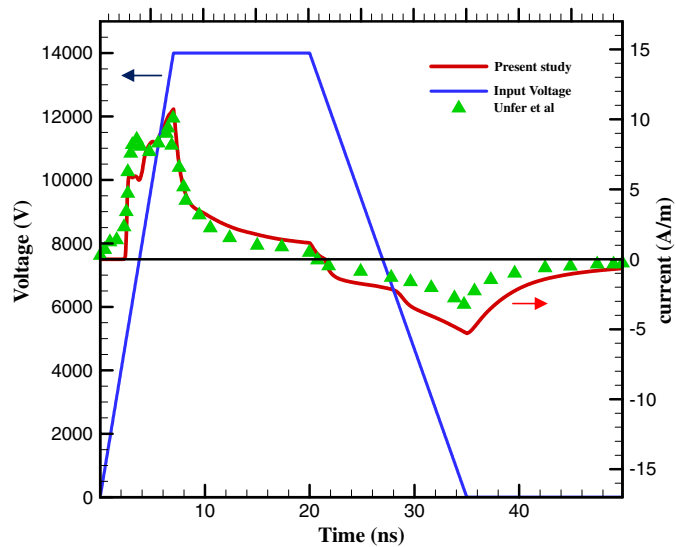


Fig. 9. Validation of the second test case for the pulsed input voltage.

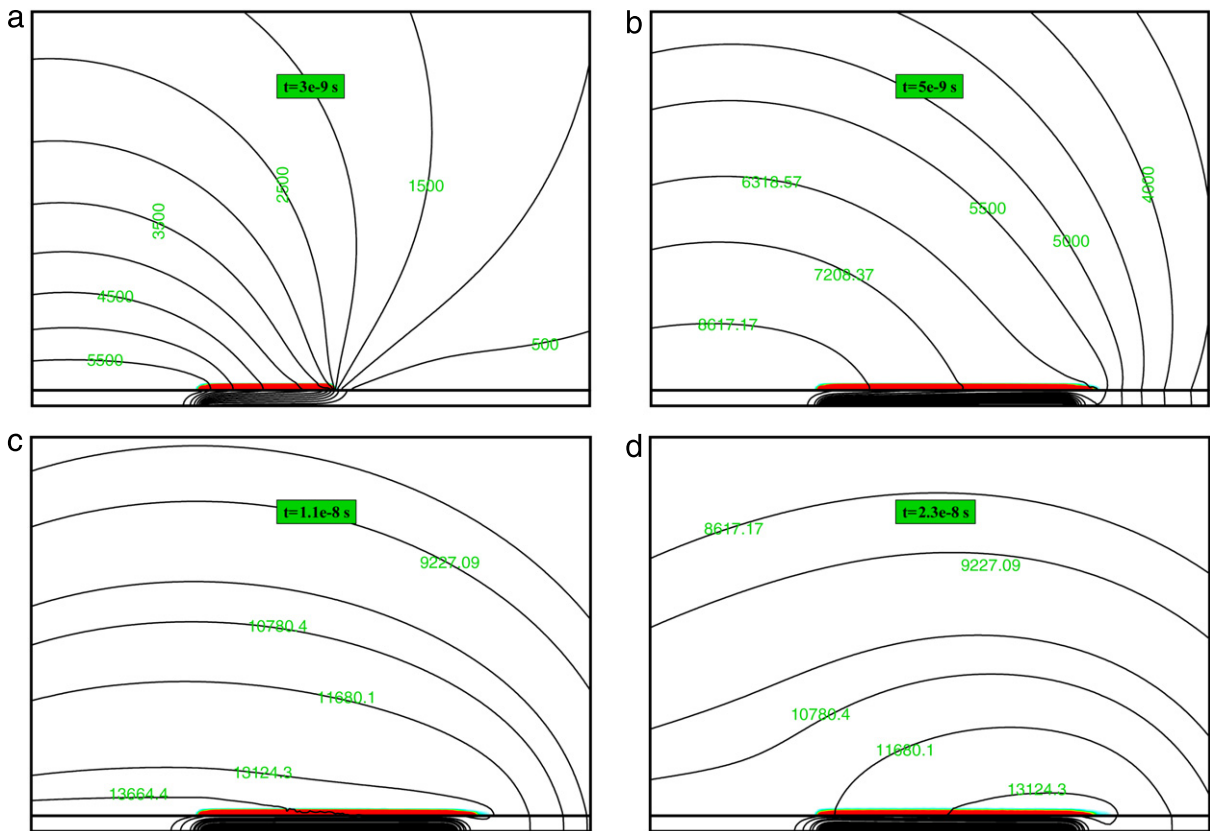
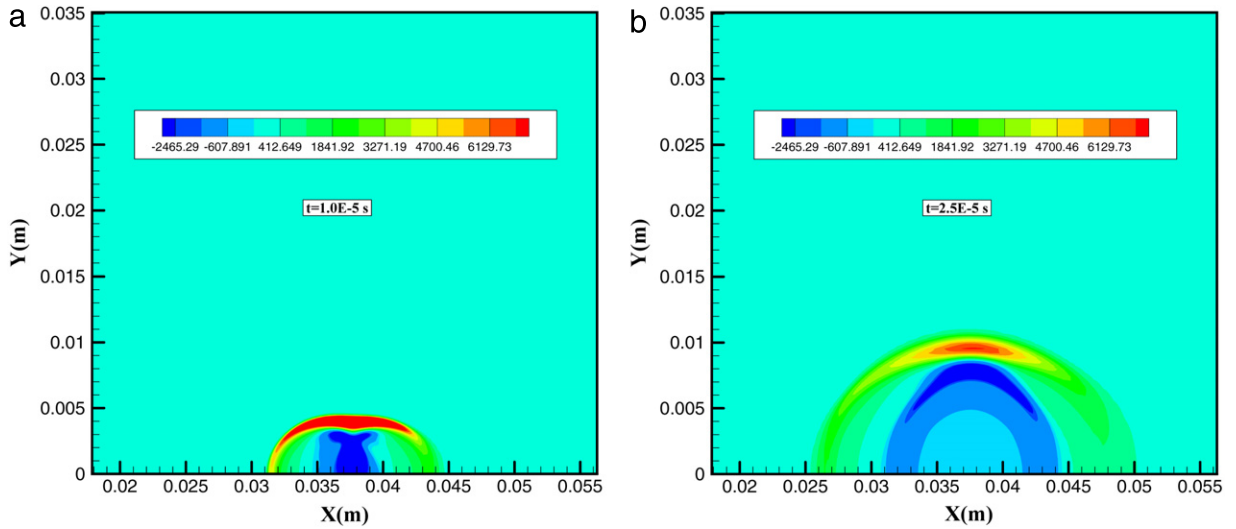


Fig. 10. Streamer formation during the voltage pulse at: (a)  $t = 3$  ns; (b)  $t = 5$  ns; (c)  $t = 11$  ns; (d)  $t = 23$  ns (values of electric potential in V).

modeling approaches is less than  $1e-3$ . The jumps in the plots represent the instants of time at which the plasma pulse is active.

Additionally, Fig. 15 shows the time variation of pressure at three different locations near the surface of the airfoil at angle of attack of  $\alpha = 20^\circ$ . The peak values show the waves that reach the probe locations. There is a small difference in the values of the wave strength seen by the pressure sign arriving at the point, for each model. This is completely natural as



**Fig. 11.** Micro-shock formation above the dielectric surface (distribution of the induced pressure difference by plasma) at: (a)  $t = 10 \mu\text{s}$ ; (b)  $t = 25 \mu\text{s}$  ( $\Delta p$  contours in (Pa)).

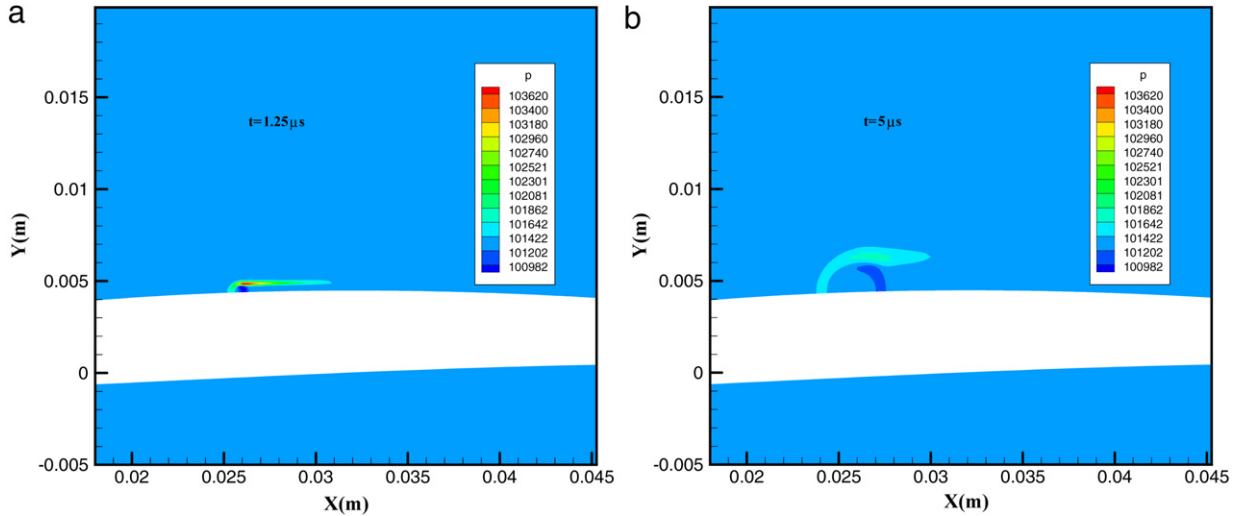


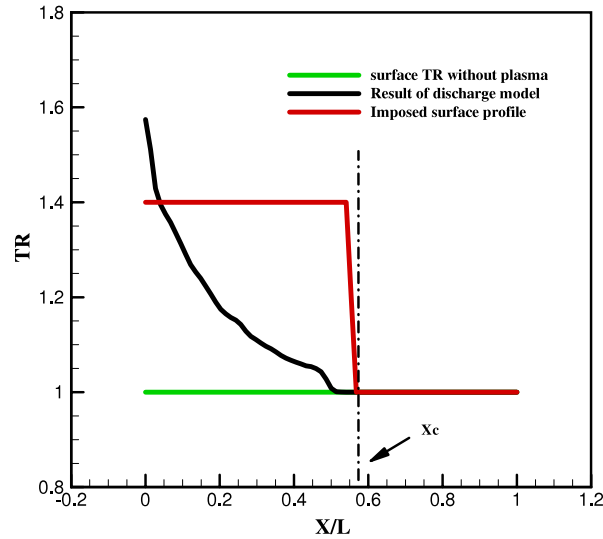
**Fig. 12.** Micro-shock wave above the dielectric surface mounted on the surface of NACA 3506 Airfoil in quiescent flow at: (a)  $t = 1.25 \mu\text{s}$ ; (b)  $t = 5 \mu\text{s}$  (pressure contours (Pa)).

the energy input and distribution in the plasma energy deposition model is not the same as in the plasma discharge model. However, the difference remains within an acceptable range.

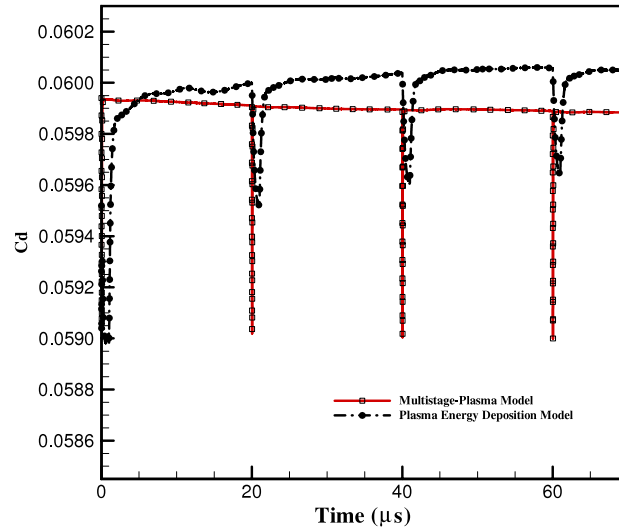
Fig. 16 compares the shape, position and strength of the plasma micro-shock wave obtained by the energy deposition model and the multistage plasma calculation approach. By comparing the contour plots, we see that the plasma energy deposition model is able to capture the plasma micro-shock wave structure with good accuracy, without the need of solving the plasma dynamics equation, for the whole duration of the calculation. In this case, there is an imposed external transonic flow ( $M = 0.75$ ) in the vicinity of the NACA 3506 airfoil, at an angle of attack of  $20^\circ$ . A micro-shock wave is formed and propagates into the flow at the speed of sound, interacting with the flow over the surface. High local density gradients whirl the heated air downstream. The combined effects of heating convection and repetitive pulse discharge lead to a modification of the flow features. The plasma micro-shock wave in the vicinity of the NACA 3506 with the angle of attack of  $20^\circ$  is shown.

Fig. 17 compares the current obtained results with the experimental results of Pescheke et al. [26]. In this figure, contour plots of pressure and density variation  $\Delta\rho = \rho^t - \rho^0$  are presented, for the purpose of comparison with the experimental results of Pescheke et al. The figure shows qualitatively the level of agreement of the current plasma calculation.

Table 1 gives the CPU time required by each model for the completion of 1 ms of simulation time for the case of the NACA 3506 airfoil. Clearly, the plasma energy deposition model is a lot less computationally expensive in comparison to other models. Although this model does not have the complexity of the others, it is still able to capture the main features of the



**Fig. 13.** Dielectric surface temperature ratio (imposed model—red line; at initial case—green line; discharge model—black line) for the NACA 3506 airfoil at  $\alpha = 4^\circ$ . (For interpretation of the references to colour in this figure legend, the reader is referred to the web version of this article.)



**Fig. 14.** Comparison of the drag coefficient obtained on the surface of the NACA 3506 airfoil at  $\alpha = 4^\circ$  by different models.

**Table 1**

Comparison of the computational time for various models.

	Plasma discharge model	Plasma multistage model	Plasma energy deposition model
CPU time for 1 ms	884 h	132 h	1.74 h

effects of NS DBD plasma actuators correctly. Thus it presents itself as a good candidate to be used for modeling large scale problems.

## 5. Conclusions

A solver for both plasma and gas dynamics, based on the transport equations of charged particles and the Navier–Stokes equations, is developed in the OpenFoam environment for modeling nanosecond plasma actuators. Based on the results of the plasma discharge model, an energy deposition model was also developed for the simulation of the effects of DBD actuators. The accuracy of the solver was tested through comparison with the available results in the literature. It was shown that fast energy transfer, from plasma to fluid, leads to the formation of micro-shock waves responsible for modifying the

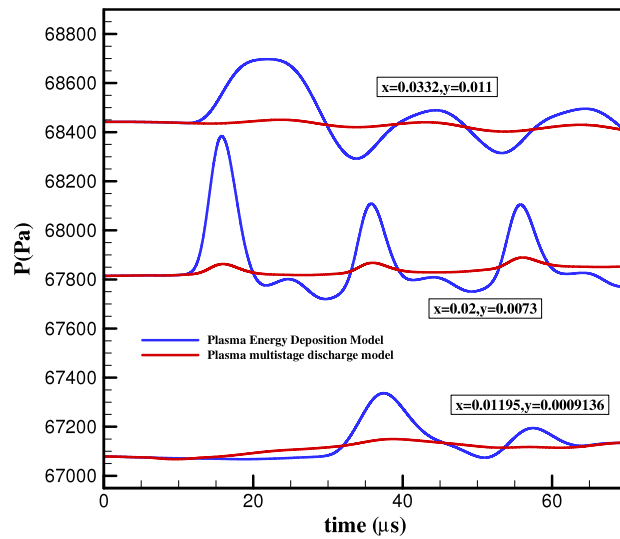


Fig. 15. Time variation of pressure at three probe locations.

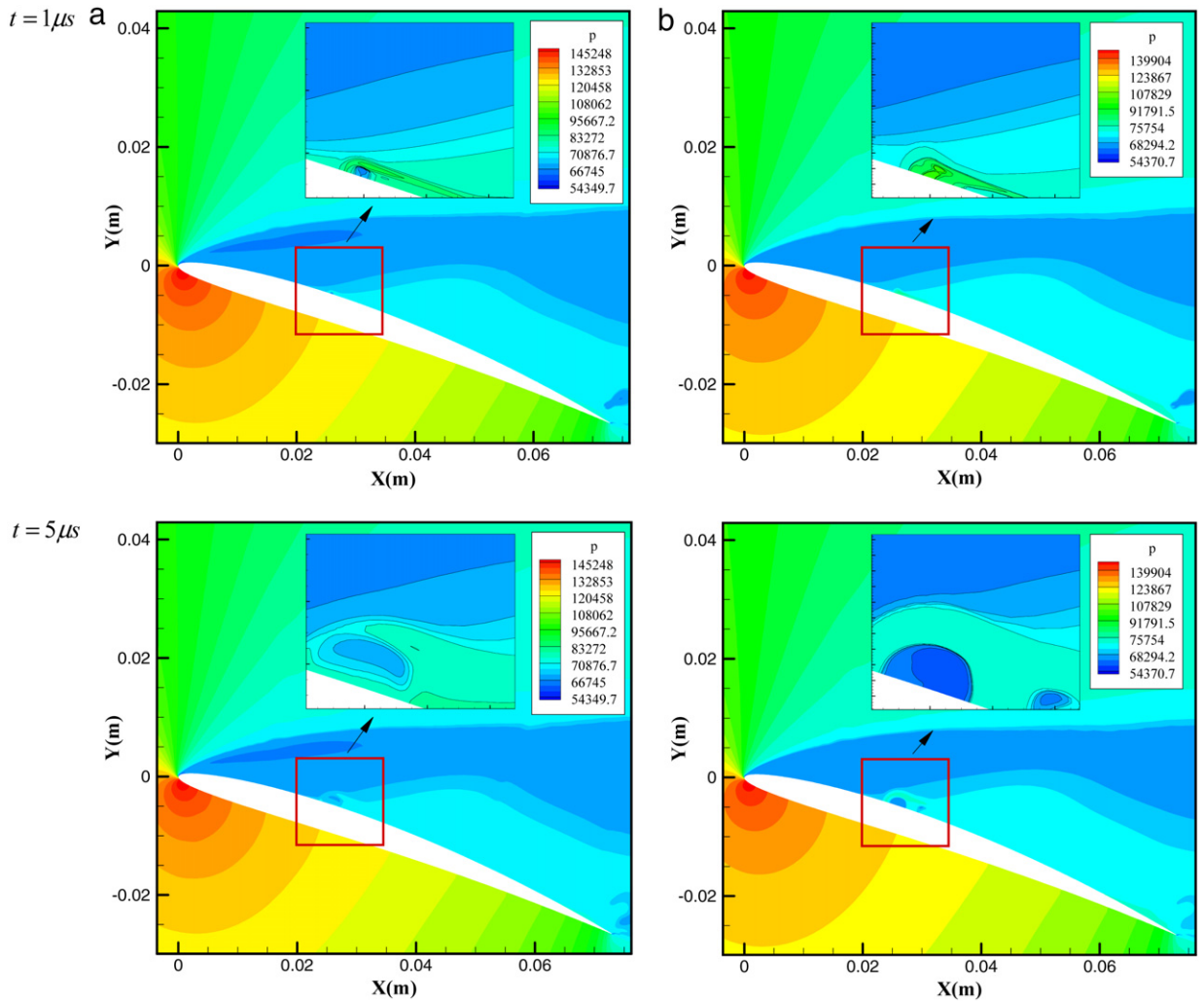


Fig. 16. Comparison the wave location and shape obtained by (a) plasma multistage solution and (b) plasma energy deposition model.



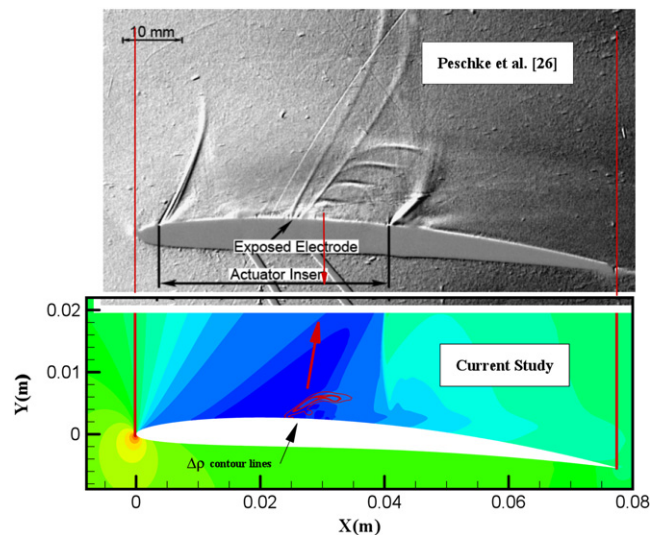


Fig. 17. Comparison of the present numerical simulation with the experimental results of Peschke et al. [26] at  $t = 10 \mu\text{s}$ .

main flow features. Also, a nanosecond plasma actuator for transonic flow over an airfoil was tested numerically. Although this model does not have the complexity of others, it was shown that it is able to capture the main features of the effect of NS DBD plasma actuators correctly, with less computational time. Thus it could be viable for modeling large scale problems when use of standard plasma discharge models is not viable.

## Acknowledgments

The present work was performed as part of Project MAAT, supported by European Union within the 7th Framework Programme under grant number 285602, and also supported by CAST—Centre for Aerospace Sciences and Technology Research Unit No. 151.

## References

- [1] A. Dumas, M. Madonia, I. Giuliani, M. Trancossi, MAAT Cruiser/Feeder Project: Criticalities and Solution Guidelines. SAE Technical Paper. 2011, p. 01-2784.
- [2] H. Nishida, T. Abe, Numerical analysis of plasma evolution on dielectric barrier discharge plasma actuator, *J. Appl. Phys.* 110 (2011) 013302.
- [3] M. Abdollahzadeh, J. Páscoa, P.J. Oliveira, Numerical modelling of boundary layer control using dielectric barrier discharge, in: MEFTTE IV Conferencia Nacional em Mecânica de Fluidos, Termodinâmica e Energia, 2012, p. 63.
- [4] M. Abdollahzadeh, J. Páscoa, P.J. Oliveira, Numerical investigation on efficiency increase in high altitude propulsion systems using plasma actuators, in: ECCOMAS European Congress on Computational Methods in Applied Sciences and Engineering, 2012, pp. 6563–6581.
- [5] A. Straikovskii, D. Roupasov, A. Nikipelov, M. Nudnova, SDBD plasma actuator with nanosecond pulse periodic discharge, *Plasma Sources Sci. Technol.* 18 (2009) 03415.
- [6] M. Abdollahzadeh, J. Páscoa, P.J. Oliveira, Two dimensional numerical modelling of micro-shock wave creation in nanosecond plasma actuators, in: FEMTEC 4th International Congress on Computational Engineering and Sciences, 2013, p. 25.
- [7] Alan R. Hoskinson, Measurements and simulations of surface dielectric barrier discharges used as plasma actuators, NASA/CR, 2012, p. 217628.
- [8] S.T. Surzhikov, J.S. Shang, Two-component plasma model for two-dimensional glow discharge in magnetic field, *J. Comput. Phys.* 199 (2004) 437–467.
- [9] T. Unfer, J.P. Boeuf, Modelling of nanosecond surface discharge actuator, *J. Phys. D: Appl. Phys.* 42 (2009) 194017.
- [10] X. Che, T. Shao, W. Nie, P. Yan, Numerical simulation on a nanosecond-pulse surface dielectric barrier discharge actuator in near space, *J. Phys. D: Appl. Phys.* 45 (2009) 145201.
- [11] C.C. Wang, S. Roy, Numerical simulation of a gas turbine combustor using nanosecond pulsed actuators, in: 51st AIAA Aerospace Sciences Meeting, 2013, 0894.
- [12] T. Unfer, J.P. Boeuf, Modelling and comparison of sinusoidal and nanosecond pulsed surface dielectric barrier discharges for flow control, *Plasma Phys. Control. Fusion* 52 (2010) 124019.
- [13] A. Flitti, S. Pancheshnyi, Gas heating in fast pulsed discharges in  $\text{N}_2/\text{O}_2$  mixtures, *Eur. Phys. J. Appl. Phys.* 45 (2009) 21001.
- [14] I. Adamovich, S.O. Macheret, J.W. Rich, C.E. Treanor, Vibrational Relaxation and Dissociation Behind Shock Waves Part2: Master Equation Modeling, in: AIAA Paper, vol. 33, 1995, pp. 1070–1075.
- [15] G.J.M. Hagelaar, L.C. Pitchford, Solving the Boltzman equation to obtain electron transport coefficients and rate coefficients for fluid models, *Plasma Sources Sci. Technol.* 14 (2005) 722.
- [16] D.V. Gaitonde, M.H. McCrink, A semi-empirical model of a nanosecond pulsed plasma actuator for flow control simulations with LES, in: AIAA paper, 2012, p. 0184.
- [17] D.V. Gaitonde, Analysis of plasma-based control mechanisms through large Eddy simulations, *Comput. & Fluids* 85 (2013) 19–26.
- [18] S.B. Leonov, D.A. Yaranatsev, V.G. Gromov, A.P. Kuriachy, Mechanisms of flow control by near-surface electrical discharge generation, in: AIAA paper, 2005, p. 780.
- [19] D. Knight, Survey of aerodynamic drag reduction at high speed by energy deposition, *J. Propul. Power* 24 (2008) 1153–1167.
- [20] P.L.G. Ventzek, R.J. Hoekstra, M.J. Kushner, Two-dimensional modelling of high plasma density inductively coupled sources for materials processing, *J. Vac. Sci. Technol. B* 12 (1994) 461–477.
- [21] J. Poggie, I. Adamovich, N. Bisek, M. Nishihara, Numerical simulation of nanosecond-pulse electrical discharges, *Plasma Sources Sci. Technol.* 22 (2013) 015001.

- [22] S. Nagaraja, V. Yang, I. Adamovich, Multi-scale modelling of pulsed nanosecond dielectric barrier plasma discharges in plane-to-plane geometry, *J. Phys. D: Appl. Phys.* 46 (2013) 155205.
- [23] P.L. Roe, Approximate riemann solvers, parameter vectors, and difference schemes, *J. Comput. Phys.* 43 (1981) 357–372.
- [24] F. Menter, J. Carregal Ferreira, T. Esch, B. Konno, The SST turbulence model with improved wall treatment for heat transfer predictions in gas turbines, in: *Proc. Int. Gas Turbine Congress, Tokyo, Nov. 2–7. IGTC2003-TS-059*.
- [25] J.P. Bouef, L.C. Pitchford, Electrohydrodynamic force and aerodynamic flow acceleration in surface dielectric barrier discharge, *J. Appl. Phys* 97 (2005) 103307.
- [26] P. Peschke, S. Goeke, Ch. Hollenstein, P. Leyland, P. Ott, Interaction between nanosecond pulse DBD actuators and transonic flow, in: *42nd AIAA Plasmadynamics and Laser Conference, AIAA, 2011*, p. 3734.
- [27] S.M. Aulchenko, V.P. Zamuraev, I.A. Znamenskaya, A.P. Kalinina, D.M. Orlov, N.N. Sysoev, On the Possibility of Controlling Transonic Profile Flow with Energy Deposition by Means of a Plasma-Sheet Nanosecond Discharge, *Technical Physics* 54 (2009) 343–353.
- [28] D.V. Roupasov, A.A. Nikipelov, M.M. Nudnova, A.Yu. Starikovskii, Flow Separation Control by Plasma Actuator with Nanosecond Pulsed-Periodic Discharge, in: *AIAA Paper*, vol. 47, 2009, pp. 168–185.